Re-entrant percolation in active Brownian hard disks
Electronic Supplementary Information

David Evans, José Martin-Roca, Nathan J. Harmer, Chantal Valeriani and Mark A. Miller

S1 Changing Péclet number via the active force

The dimensionless Péclet number $\mathrm{Pe} = 3F_\mathrm{a}D_\mathrm{t}/\sigma k_\mathrm{B}TD_\mathrm{r}$ can be systematically varied in several ways. The results in Fig. 2(b) of the main text have been produced by changing the rotational diffusion constant D_r. We have also tested the behaviour of the system when Pe is changed by varying the propulsion force, F_a.

Figure S1 compares the dependence of the percolation threshold of two-dimensional active Brownian particles (ABPs) on the Péclet number when Pe is controlled by varying the rotational diffusion coefficient and the propulsion force. The two curves have the same qualitative shape, with a minimum in the threshold between $\mathrm{Pe} = 10$ and $\mathrm{Pe} = 15$. In the case where the Péclet number is changed by varying the propulsion force, the motility-induced phase separation (MIPS) boundary occurs at a lower Péclet number than in the case where it varies with the rotational diffusion coefficient,[1] and so it is not possible to probe the percolation threshold beyond $\mathrm{Pe} = 30$ within the one-phase regime.

S2 Dependence of percolation on the connectivity distance

In the main article we chose a connectivity distance of $\lambda = 1.3$. This value gives percolation in a density regime where we may study a large interval of Pe without encountering MIPS. To test the sensitivity of our results, we have also calculated the percolation threshold at different connectivity distances as shown in Figure S2. Re-entrant percolation is observed for connectivity distances in the range $1.2 \leq \lambda \leq 1.4$.

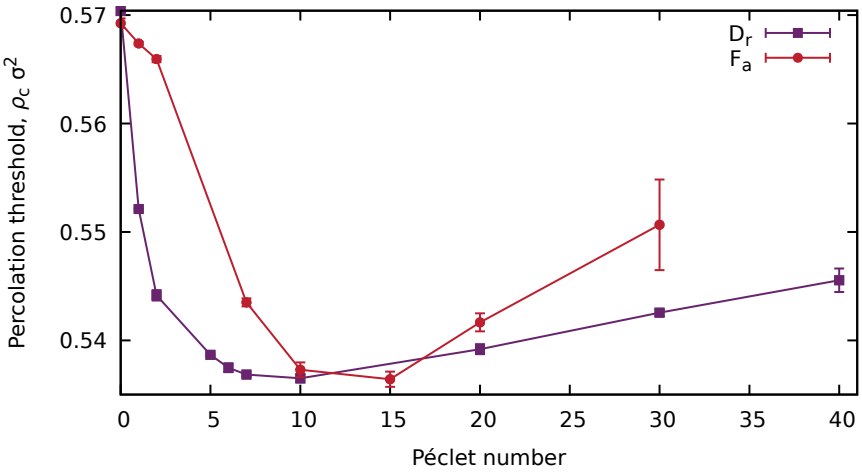

Figure S1: Percolation threshold versus Péclet number for active Brownian particles where the activity is changed using the rotational diffusion D_r or by the propulsion force F_a.

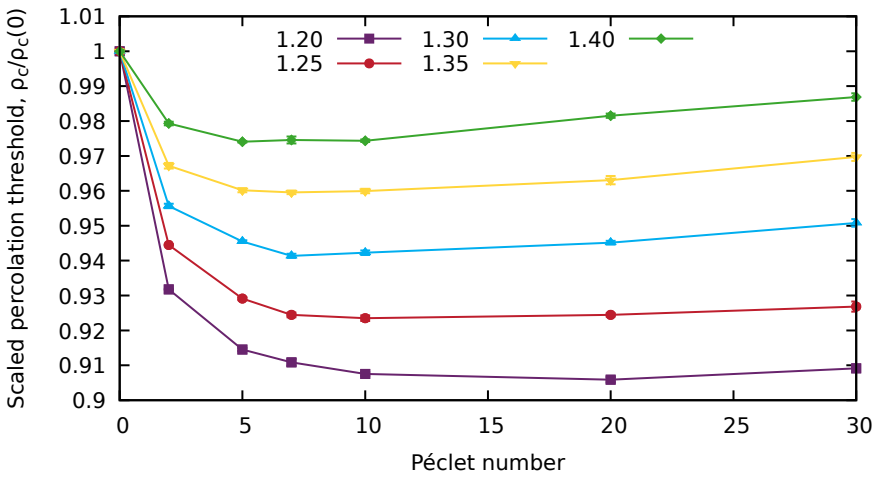

Figure S2: Percolation threshold as a function of Péclet number at different values of the connectivity distance, $\lambda\sigma$. Each curve is scaled by the threshold at $\mathrm{Pe} = 0$.

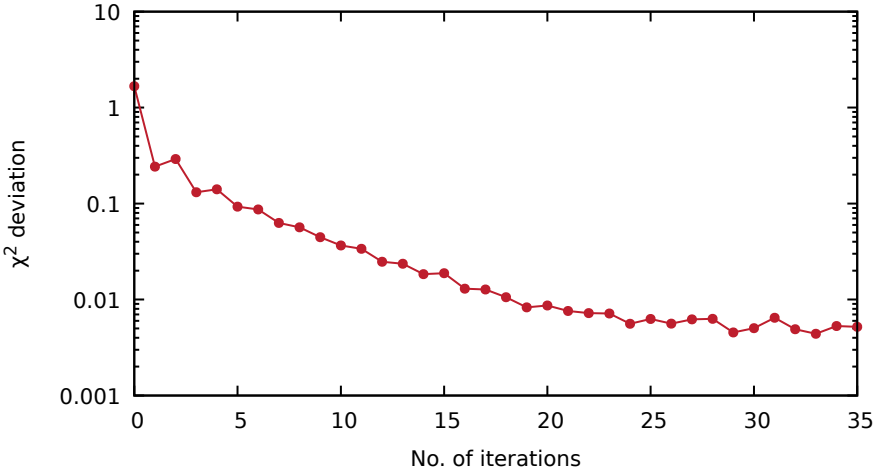

Figure S3: The total square deviation, χ^2, between the target radial distribution function and the radial distribution function from the trial potential at each iteration of IBI at $\mathrm{Pe} = 2$.

S3 Convergence of iterative Boltzmann inversion

After each iteration of the iterative Boltzmann inversion (IBI) scheme, we calculate the sum of the squared deviations between the target radial distribution function (RDF) and the RDF from that iteration's simulation as

$$\chi^2 = \sum_i \left[g\left(r_i\right) - g_{\mathrm{target}}\left(r_i\right) \right]^2 . \tag{S1}$$

We terminate the iterative scheme when the value of χ^2 levels out and successive iterations do not improve the trial potential. Figure S3 shows χ^2 for each iteration during IBI for $\mathrm{Pe} = 2$ where convergence is reached within 35 iterations.

S4 Percolation threshold of square-well disks

We have measured the percolation threshold of passive hard disks with a square-well potential (Eq. 7 in the main article) as one of the simplest models with conservative attractive interactions. The passive simulations were carried out using the standard Metropolis Monte Carlo (MC) algorithm with single-particle moves.

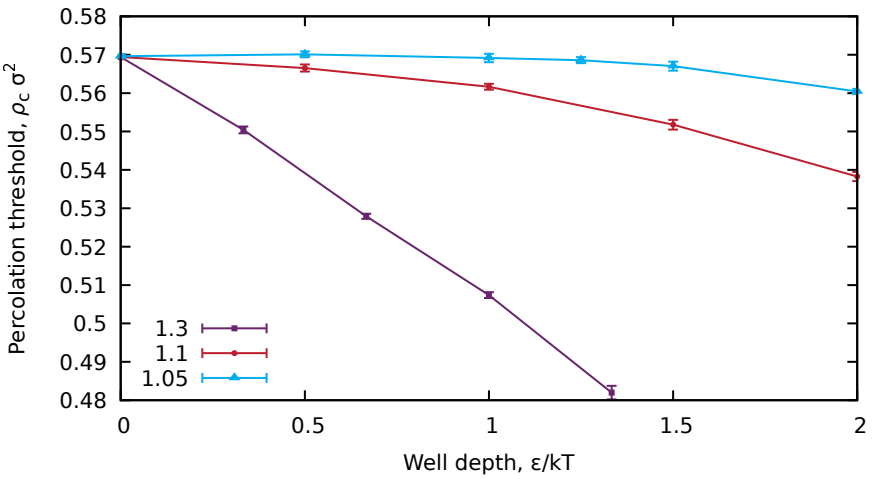

Figure S4: Percolation threshold as a function of square-well well depth for different square well ranges λ_{SW} of 1.3, 1.1 and 1.05 and constant connectivity distance $\lambda = 1.3$. The percolation threshold decreases monotonically as the level of attraction in the system increases.

As seen in Fig. S4, the percolation threshold is a monotonically decreasing function of increasing well depth for all values of the square-well attraction range λ_{SW} at a fixed connectivity range of $\lambda = 1.3$. As in our characterisation of active systems, where we restrict our study of percolation to the one-phase region before MIPS, here we do not enter the gas–liquid phase-separated region of the phase diagram, which occurs above $\epsilon/k_{\mathrm{B}}T = 1.3$.

S5 Mapping active disks onto passive square-well disks

The effective potentials produced by iterative Boltzmann inversion, seen in Fig. 4(b) of the main text, are attractive with a pseudo-hard core repulsion. Both the depth and the range of the attraction evolve with increasing activity. To make a link with the square-well potential, we can match the depth of the effective potential of the ABP to the square-well depth parameter ϵ_{SW} (Eq. 7 of the main text) and then determine the square-well range λ_{SW} by equating the second virial coefficients B_2. In general in two dimensions for particles interacting via pairwise potential $V(r)$,

$$B_2 = -\frac{1}{2}\int_0^\infty \left[\exp\left(\frac{-V(r)}{k_{\mathrm{B}}T}\right) - 1\right] 2\pi r dr. \tag{S2}$$

For the square well, the result is

$$B_2 = -\frac{\pi\sigma^2}{2}\left[\left(e^{\epsilon_{\mathrm{SW}}/k_{\mathrm{B}}T} - 1\right)\left(\lambda_{\mathrm{SW}}^2 - 1\right) - 1\right]. \tag{S3}$$

Inverting yields

$$\lambda_{\mathrm{SW}} = \sqrt{\frac{2B_2/\pi\sigma^2 - \exp\left(\epsilon_{\mathrm{SW}}/k_{\mathrm{B}}T\right)}{1 - \exp\left(\epsilon_{\mathrm{SW}}/k_{\mathrm{B}}T\right)}}, \tag{S4}$$

which can be evaluated by substituting the numerically integrated B_2 from the ABP effective potentials.

The effective second virial coefficient as a function of Pe is shown in Fig. S5(a). As expected, B_2 decreases monotonically with increasing activity, changing from positive to negative when the effective attraction dominates over the repulsive core. The effective square well range is plotted in Fig. S5(b). By about Pe = 2, it has settled down at $\lambda_{\mathrm{SW}} = 1.23$. Beyond that point the ongoing decrease in B_2 arises from further deepening of the effective potential rather than broadening of the interaction range.

S6 Characterising structural differences

Iterative Boltzmann inversion (IBI) found pairwise potentials that reproduced the radial distribution function $g(r)$ very well. However when a MC simulation was performed with the resulting potentials,

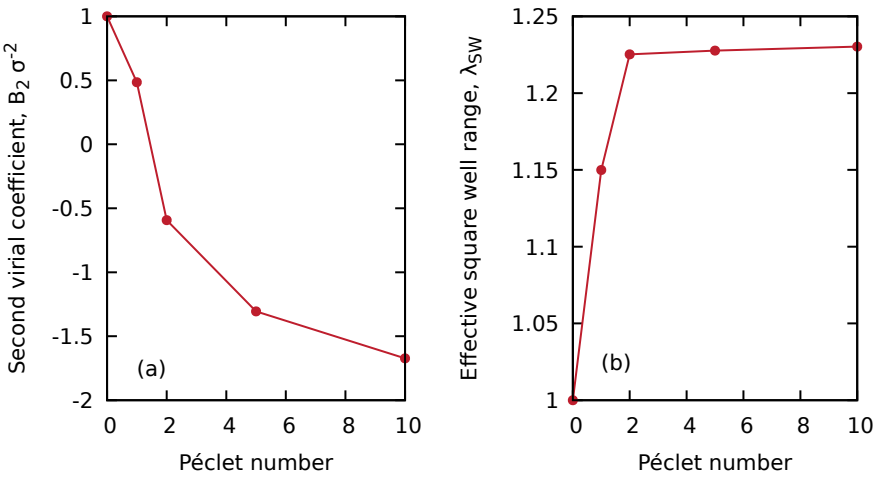

Figure S5: (a) The effective second virial coefficient B_2 of ABPs as a function of Péclet number, calculated from the effective potentials derived from iterative Boltzmann inversion. (b) The effective square-well range λ_{SW} as a function of Péclet number calculated from B_2 and the mapping in Eq. S4.

the percolation properties were not accurately reproduced, implying that many-body interactions are significant. We have calculated a number of structural quantities to characterise the differences between the active and passive systems.

S6.1 Coordination number

As defined in the main text, the coordination number is the number of particles that are connected to a given particle. We consider particles to be connected if their centres are separated by less than $\lambda\sigma = 1.3\sigma$. The mean coordination number per particle $\langle n \rangle$ is averaged over all particles and sampled configurations, and gives a measure of the local connectivity in the steady state.

Figure S6 shows the mean coordination number as a function of activity at a constant density of $\rho = 0.54\sigma^{-2}$ for the active and the mapped passive systems. The passive data are from MC simulations using the effective potentials produced using IBI up to $\mathrm{Pe} = 10$, beyond which IBI fails to return an effective potential that accurately reproduces $g(r)$ from the active simulations. The mapped passive system reproduces the mean coordination number of ABPs well, as might be expected because coordination number is closely related to the first peak of $g(r)$, which we know to be accurately captured by the effective potential.

S6.2 Radius of gyration

The radius of gyration R_{g} of a cluster is the root mean squared distance of particles from the cluster's centre of mass:

$$R_{\mathrm{g}}^2 = \frac{1}{s}\sum_{i}^{s} |\mathbf{r}_i - \mathbf{r}_{\mathrm{cm}}|^2 \,, \tag{S5}$$

where $\mathbf{r}_i$ is the position of the ith particle in the cluster, and $\mathbf{r}_{\mathrm{cm}}$ is the position of the centre of mass, $\mathbf{r}_{\mathrm{cm}} = s^{-1}\sum_i^s \mathbf{r}_i$.

Figure S7 shows the mean radius of gyration $\langle R_{\mathrm{g}} \rangle$ as a function of cluster size for the active and passive systems at $\mathrm{Pe} = 2$ and $\rho = 0.54\sigma^{-2}$. Percolating clusters are excluded from the average, since they represent infinite clusters once the periodic boundary conditions are considered. Statistics are gathered for each cluster size up to $s = 10$ in steps of 1. Thereafter, clusters are averaged over a range of sizes with the lower edge of each bin obtained by multiplying the previous edge by 1.6. The geometrically increasing bin width compensates for the increasingly rarity of larger clusters and produces a regular spacing on a logarithmic axis.

Over about two decades, $10 \lesssim s \lesssim 1000$, R_{g} scales approximately as $s^{0.5}$, as expected for non-fractal clusters in two dimensions. Larger cluster sizes are more strongly affected by the finite size of

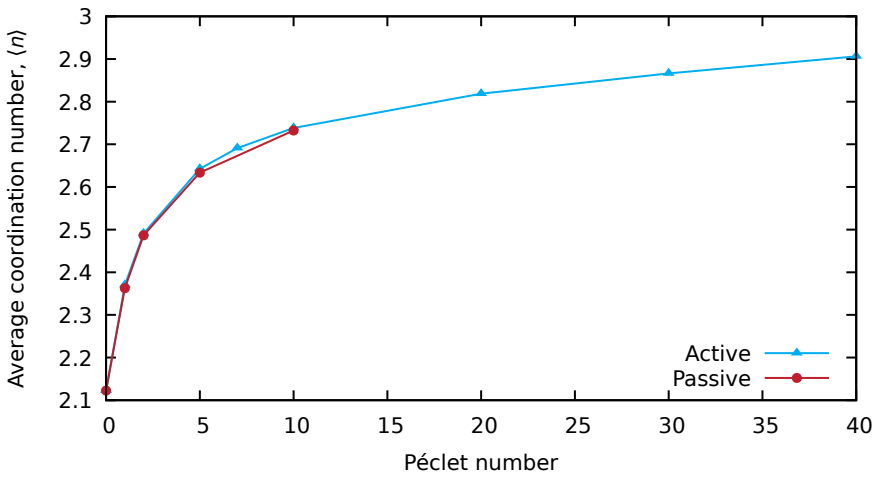

Figure S6: Average coordination number $\langle n \rangle$ as a function of Péclet number at $\rho = 0.54\sigma^{-2}$ for active and passive systems. The passive data are from MC simulations using the effective potentials from IBI and stop at Pe = 10, after which an accurate effective potential cannot be obtained.

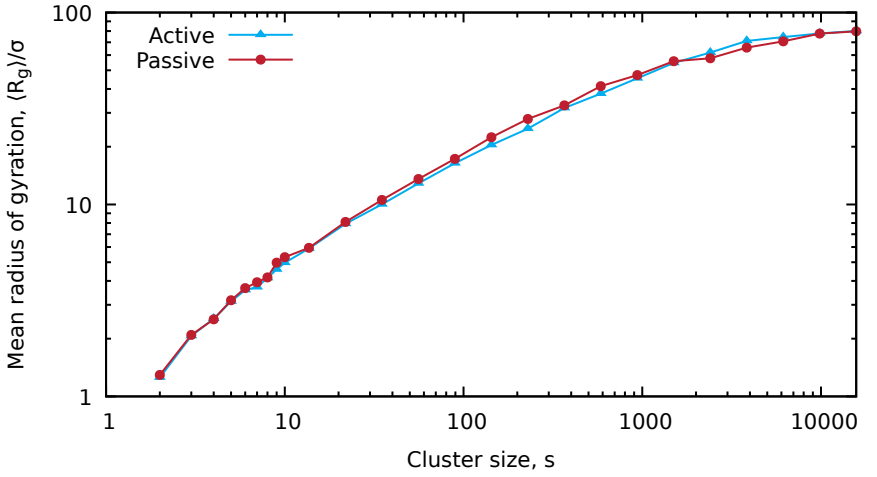

Figure S7: R_g, for clusters of size s for the passive and active systems at Pe = 2 and $\rho = 0.54\sigma^{-2}$.

the simulation cell since the average is restricted to clusters that contain many particles but do not connect across the periodic boundary conditions and therefore are likely to have a smaller average radius of gyration than free clusters with the same number of particles in a larger cell. Deviations between the R_g distributions of the passive and active cases are small, but we note that percolation is very sensitive to details of cluster shape; at the percolation threshold itself, connectivity of a given cluster may be gained or lost by a small displacement of a single particle.

S6.3 Cluster size distribution

Let n_s be the probability that a randomly chosen cluster contains s particles and does not percolate. The probability that a randomly chosen particle belongs to a non-percolating cluster of size s is then sn_s. Fig. S8 shows both definitions of the cluster size distribution. As in the calculation of the radius of gyration in Sec. S6.2, logarithmic binning is applied (but here starting from $s = 50$).

As demonstrated by the black line in Fig. S8(b), n_s follows the normal scaling $n_s \sim s^{-\tau}$ away from the critical density, with the expected value of the exponent $\tau = 187/91$ in two dimensions.[2] The active and passive distributions are barely distinguishable. The particle-based distribution sn_s in Fig. S8(a) highlights small differences for clusters larger than $s = 100$. Naturally, it is the largest clusters that we expect to influence the onset of percolation most strongly.

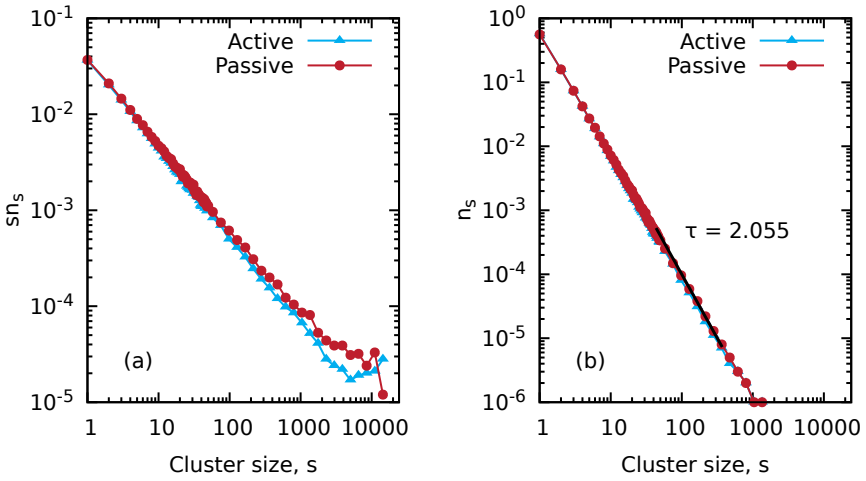

Figure S8: Cluster size distributions, (a) sn_s and (b) n_s, both at $\rho = 0.54\sigma^{-2}$ and Pe = 2 for the active and passive systems. The black line in (b) shows the accepted value of the critical exponent [2] for the cluster size in two dimensions, $\tau = 187/91$.

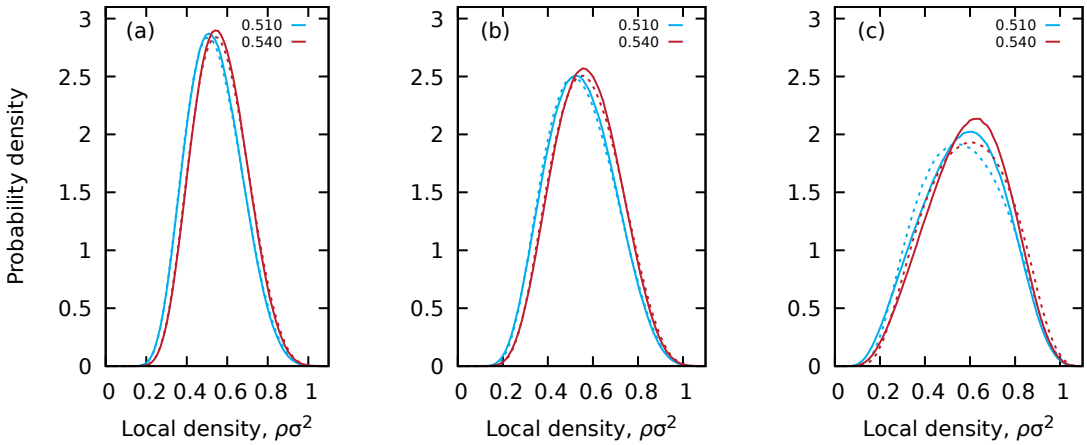

Figure S9: The local density distributions calculated as the inverse Voronoi area at $\rho = 0.51\sigma^{-2}$ and $\rho = 0.54\sigma^{-2}$ for (a) Pe = 1, (b) Pe = 2, and (c) Pe = 10. Solid lines are passive systems and dashed lines are active systems.

S6.4 Local density distribution

A Voronoi analysis of a configuration associates an area with each particle, the inverse of which is a measure of the local density at that point. The distributions of this local density for the active and passive systems at two number densities are shown in Fig. S9.

Agreement is good but not perfect even at the lowest activity of Pe = 1. The discrepancies increase with activity and are more prominent at the higher density. Hence, the Voronoi analysis reveals discernible differences in the local structure, despite the accurate reproduction of the mean coordination number (Fig. S6).

S6.5 Conditional nearest neighbour distribution function

Given a circular region of space of radius r that does not contain any particle centres, the probability that a particle centre lies in a shell of thickness dr around this area is $2\pi r\rho G_V(r)dr$,[3,4] where $G_V(r)$ is the conditional nearest neighbour distribution. $G_V(r)$ can formally be expressed in terms of two- and many-body correlation functions of the structure[3,4] and is therefore one way to detect any difference in

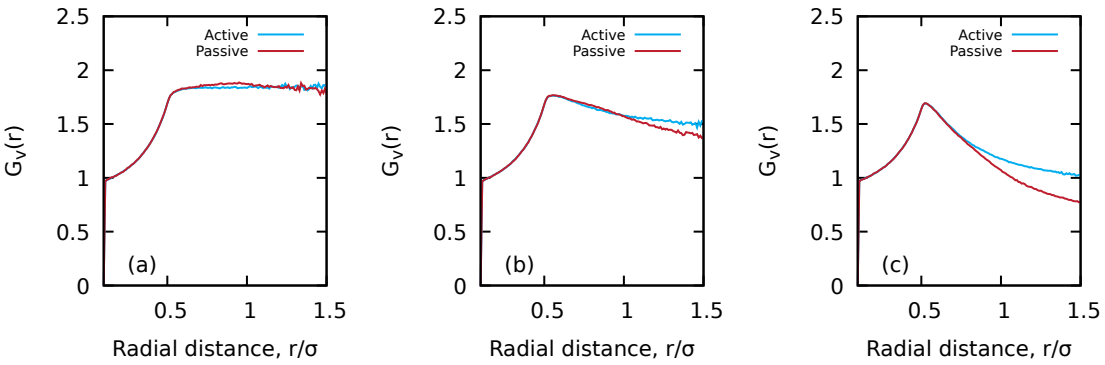

Figure S10: Comparison of the conditional nearest neighbour distributions, $G_V(r)$, of the active and passive systems for (a) Pe = 1, $\rho = 0.55\sigma^{-2}$, (b) Pe = 2, $\rho = 0.545\sigma^{-2}$, and (c) Pe = 10, $\rho = 0.525\sigma^{-2}$.

structure beyond pairwise functions like $g(r)$.

Fig. S10 shows $G_V(r)$ for three different Péclet numbers, each evaluated at the density where there is the biggest difference in percolation probability between the active and mapped passive simulations. Up to $r = 0.5\sigma$, $G_V(r)$ is fully determined by the density, since a circular region with diameter smaller than the particle diameter cannot contain more than one particle centre if the particles are impenetrable. Hence, the initial part of $G_V(r)$ is identical for the active and passive simulations in each case.

For $r > 0.5\sigma$, however, differences between the active and passive systems are readily seen with increasing Pe, indicating the presence of many-body correlations in the active system that are absent (by construction) in the passive simulations with the effective pairwise potential. We note that the range of these differences is only on the order of a particle diameter, demonstrating that the structure of the active system differs even at this local scale from the passive system, even though their pairwise structures, as measured by $g(r)$ are virtually identical.

References

[1] J. Martin-Roca, R. Martinez, L. C. Alexander, A. L. Diez, D. G. A. L. Aarts, F. Alarcon, J. Ramírez and C. Valeriani, *J. Chem. Phys.*, 2021, **154**, 164901.

[2] D. Stauffer and A. Aharony, *Introduction to Percolation Theory*, Taylor and Francis, Revised 2nd Edition edn, 1994.

[3] S. Torquato, B. Lu and J. Rubinstein, *Phys. Rev. A*, 1990, **41**, 2059–2075.

[4] H. Wang, F. H. Stillinger and S. Torquato, *J. Chem. Phys.*, 2020, **153**, 124106.